Thermal regime of Blake Ridge using seismic and borehole data

Enter authors here: Arka Dyuti Sarkar[1], and M. Huuse[1]

[1]Department of Earth & Environmental Sciences,University of Manchester, Williamson Building, Oxford Road, Manchester M13 9PL, UK.

Corresponding author: Arka Dyuti Sarkar (arkadyuti.sarkar@manchester.ac.uk)

Key Points:

- Non-invasive thermal regime characterization methodology utilizing seismic data.
- Testing in the Blake Ridge hydrate province expands subsurface temperature profile beyond existing data.
- Borehole velocity data has been used to condition an empirical subsurface thermal conductivity model.

Abstract

Constraining the subsurface thermal regime is of importance not just to the offshore hydrocarbon exploration industry but also for understanding the geothermal regime in context of microbiological activity. This regime is tested through the use of seismic data to noninvasively estimate subsurface temperatures through the identification of bottom simulating reflectors (BSRs) at the base gas hydrate stability zone (GHSZ) to mark out an isotherm. This reflection seismic thermometry methodology is applied to the Blake Ridge, offshore east coast USA, where ODP Leg 164 boreholes provide temperature data required for thermal model constraints. 3D thermal modelling using reflection seismic data is used to examine the lateral variability of the shallow thermal regime while 1D thermal modelling is applied to ODP Sites 994, 995 and 997. The resulting estimated subsurface temperature profiles had a margin of error of 13.9% compared to in situ temperature measurements recorded from the boreholes. This method of thermal modelling could significantly expand the application of thermal data from ODP sites to areas covered by seismic data, which would considerably benefit researchers worldwide in industry and academia.

Plain Language Summary

The Blake Ridge has extensively been studied for gas hydrates. As such it serves as an excellent location to test a seismic led approach to subsurface thermal regime characterization that the authors previously developed using data from the Lüderitz Basin, offshore Namibia.

1 Introduction

Constraining the subsurface thermal regime allows the estimation of heat available for low temperature diagenetic processes and microbial incubation (Fuchs & Balling, 2016; Purkamo et al., 2020). It also allows the evaluation of advection in local heat transport. Understanding the distribution of temperature in the subsurface is important to the geothermal energy industry and in particular the energy sector, for hydrocarbon generation is greatly dependent on temperature conditions (Bonté et al., 2012; Hunt, 1984; Thompson, 1979). Present day thermal data in the subsurface is traditionally acquired using measurement probes lowered into a borehole (Lucazeau et al., 2004). Ocean Drilling Program (ODP) borehole logging data often contains a thermal data suite, characterizing parameters such as temperature, geothermal

gradient, thermal conductivity and heat flow (Popov et al., 1999; Pribnow et al., 2000). This presents a globally available subsurface thermal database accessible for researchers worldwide. However, in the absence of boreholes, it becomes difficult to determine the thermal regime in offshore domains. Seismic data enables visualization of subsurface physical features, but it can also be used to derive thermal data. Phenomena known as bottom simulating reflectors (BSRs) occur at the phase boundary for stable gas hydrate, and represent an isotherm due to hydrate stability being controlled primarily by temperature and pressure conditions (Serié et al., 2017; Shankar et al., 2014; Yamano et al., 1982). The Blake Ridge has been studied for nearly thirty years as an area of interest for gas hydrate research (Paull & Dillon, 1981). The area contains numerous indicators on seismic for the presence of gas hydrate including most importantly, BSRs. The authors have previously developed a methodology to determine present day subsurface temperatures from seismic data on a continental margin with a visible BSR (Sarkar, 2020). Testing this methodology in the Blake Ridge allows calibration of the temperature modelling process against the abundant thermal data records published as part of ODP Leg 164.

1.1 Geological setting

The Blake Ridge is located on the southeastern US passive margin offshore the South Carolina coast (Fig. 1). This physiographic feature is a Neogene and Quaternary sediment drift deposit formed from the erosion of the Blake Plateau (Burwicz & Rüpke, 2019; Wood & Ruppel, 2000). Evidence for the effects of sediment reworking through bottom currents is seen from sediment wave fields and erosional scouring of the seabed on the southern flank of the Blake Ridge (Fig. 1b) (Burwicz & Rüpke, 2019; Hornbach et al., 2008). The Western boundary undercurrent (WBUC) sweeps southward along the continental slope encountered here and mixes with the Gulf Stream at bottom water depths. This acts as a control on topography (Hornbach et al., 2003). Drilling results reveal the sediments in this area to be homogeneous and dominated by clays ranging from nannofossil clays, claystones and fine grained mudstones (Holbrook et al., 1996). Sediments at Blake Ridge are rich in organic carbon with organic matter having a mainly marine signature (Paull et al., 2000). Evidence from recovered cores indicates sedimentation rates were progressively higher going back to the Pliocene (Burwicz & Rüpke, 2019).

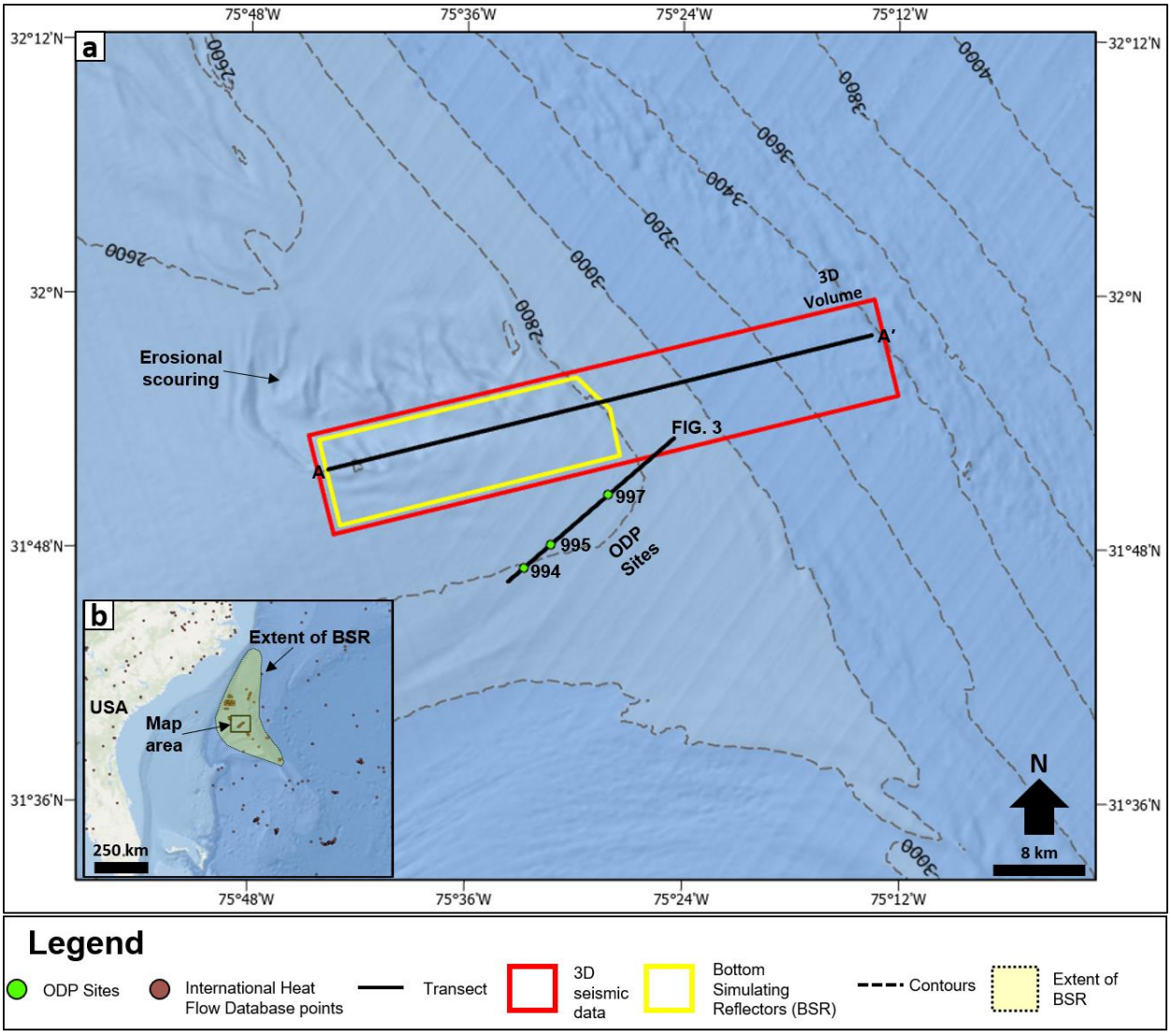

Figure 1. (a) Bathymetric map highlighting Blake Ridge study area offshore Carolina coastline with extent of the study area, mapped BSR and ODP Led 164 Sites for reference. Erosional scouring of seabed coincides with buried sediment wavefield. ODP Site 997 is located on the crest of the ridge structure. (b) Inset map of eastern US seaboard indicating study area location in context of published BSR extent. International Heat Flow Commission (IHFC) database points both onshore and offshore give an idea of thermal data coverage in the literature. Adapted from (Becker et al., 2009; Gardner, 2013; Hornbach et al., 2003; C. K. Paull & Matsumoto, 2000; Ryan et al., 2009)

Drilling in this area down to a maximum depth of 750 m below the sea floor found intermittent filling of the pore space with hydrates (Paull & Matsumoto, 2000). The occurrence of hydrates has been noted in some instances as greyish concentrated nodules at Site 994, although in Site 995, it is fine grained and dispersed in the host sediment (Paull et al., 1996c).

The sediment homogeneity in the Blake Ridge (Fig. 2a), combined with the tectonic inactivity, stable seafloor conditions and lack of structural complexity have made this area attractive for the study of the impact of gas hydrate presence on seismic response (Hornbach et al., 2008).

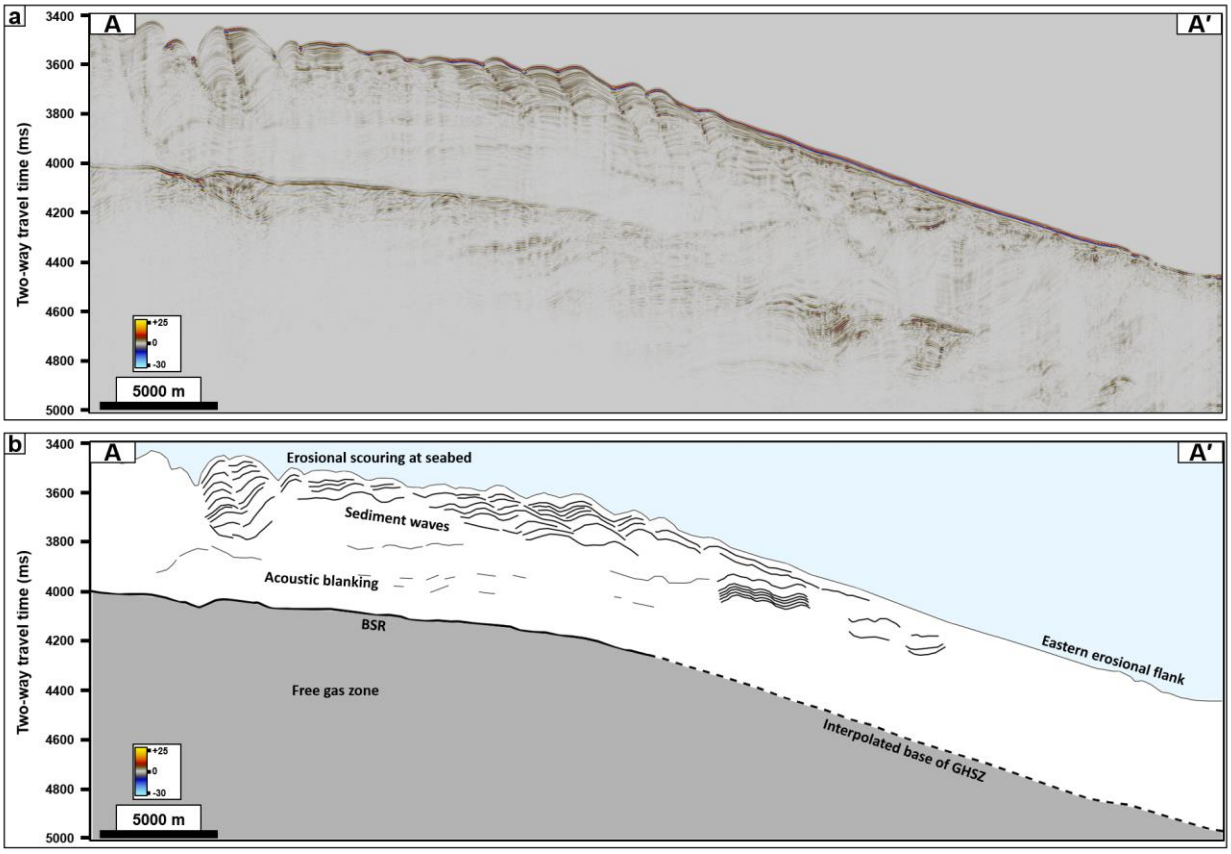

Figure 2. (a) Seismic transect A-A' from Blake Ridge (see Fig. 1a) with key features visible such as erosional scouring of seabed; sediment waves and characteristic gas hydrate related BSR. Some studies have noted the existence of scattered, deeper bright spots occurring below the BSR, which are surmised to be gas pockets (Hornbach et al., 2003). (b) Schematic view seismic

transect of A-A' from Blake Ridge adapted from (Hornbach et al., 2008) with interpolated gas hydrate stability zone (GHSZ).

1.2 Gas hydrates and bottom simulating reflectors at the Blake Ridge

Gas hydrates are naturally occurring frozen crystallographic lattices of ice trapping a guest gas molecule (Kvenvolden, 1985; Sloan et al., 1998). Gas hydrates form under elevated pressure and low temperature conditions, thus being observed onshore in permafrost at high latitudes as well as in the marine domain (Kvenvolden & Lorenson, 2001; Ruppel & Kessler, 2017). Marine gas hydrate deposits are primarily located along continental margins at water depths exceeding ~300 m and sufficiently low bottom water temperature. Gas hydrates form clathrate structures which are characterized into three subtypes (Sassen & MacDonald, 1994). Gas hydrates at Blake Ridge are mainly structure I hydrates, the most commonly occurring variety. The gases trapped within these clathrate cages are mostly hydrocarbons, with cage size determining the length of the carbon chain that can be accommodated (McConnell & Kendall, 2002). Methane is the most common trapped gas within gas hydrates and this is also found to be the case in the Blake Ridge (Paull & Dillon, 2001). Minor quantities of other gases such as carbon dioxide may also be found. The methane is either sourced locally from the biogenic breakdown of organic matter in the shallow subsurface or thermogenically from deeper sources (Sassen et al., 2001; Serié et al., 2017). Trapped gases have an isotopic and molecular signature suggestive of a microbial origin for hydrocarbon molecules (Burwicz & Rüpke, 2019; Paull et al., 1996a). Chloride ion excursions measured from pore water recovered from sediment core samples are a strong geochemical indicator for the presence of gas hydrates (Holbrook et al., 1996). The occurrence of gas hydrate zones across the Blake Ridge is supported by the similarity in chloride profiles with characteristic negative excursions across all three ODP Leg 164 sites (Paull et al., 1996a).

Geophysical detection of gas hydrates is commonly done through the identification of markers known as BSRs, which are often considered the most robust evidence of gas hydrate presence (Shipley & Houston, 1979). A BSR is a seismic event that mimics seafloor morphology whilst appearing to cross cut sedimentary strata (Calvès et al., 2008; Holbrook, 2001; Paganoni et al., 2016). The depth at which the BSR is observed is where the temperature is in excess of the

hydrate stability field, causing the frozen gas hydrate to break down to water and gas (Hornbach et al., 2003). As such the BSR is attributed as a marker for the base of the GHSZ (Fig. 2b) (Haacke et al., 2007). It is distinct in having reverse seismic polarity to the seabed as a consequence of a reduction in acoustic impedance moving from frozen gas hydrate bearing sediment above the GHSZ into free gas or water bearing sediment below (Kvenvolden & Lorenson, 2001). The presence of free gas at the hydrate phase boundary is believed to be the principal control on the amplitude of the observed BSR (Holbrook et al., 1996). Blanking can be used as a qualitative indicator of increased hydrate concentration in some cases of strata with uniform lithology displaying lateral seismic reflection amplitude contrasts above the BSR (Hornbach et al., 2003).

1.3 Discrepancies in the GHSZ

A key source of debate following ODP Leg 164 site investigations has been the discrepancies between the observed base of GHSZ and thermodynamic base of GHSZ as predicted from phase relationships. ODP Sites 955 and 997 display BSR at depths (~ 440 mbsf) (Fig. 3a) far above the estimated thermodynamic depth for the base GHSZ (~520 mbsf). One hypothesis explaining these inconsistencies is detailed below.

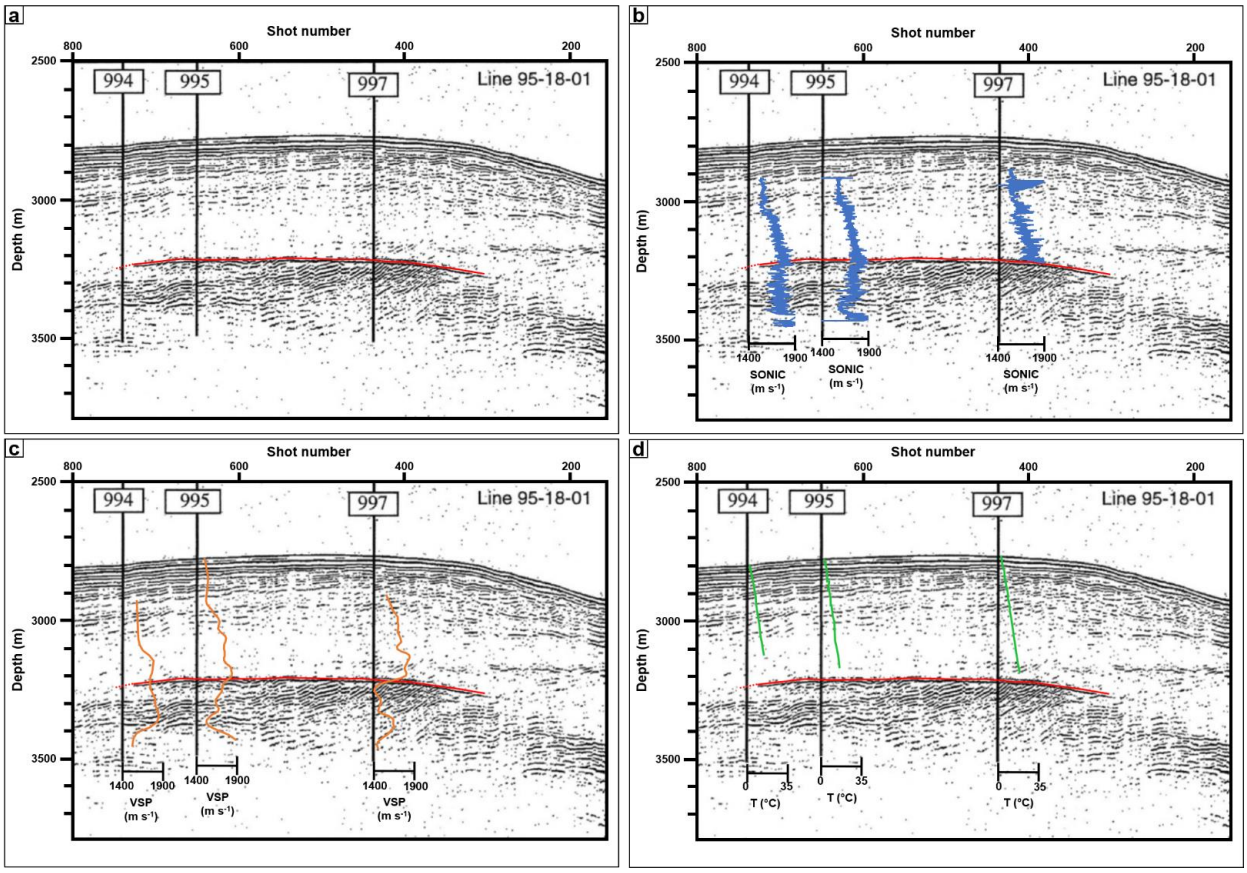

Figure 3. (a) 2D seismic reflection profile displaying relative positions of ODP Sites with BSR position marked in red (dashed line is extrapolation of BSR not observed at Site 994 on the basis of trend). High amplitude reflectors corresponding to free gas charged sediments are observed below clear BSR in Sites 995 and 997. Panels overlain with ODP data for (b) sonic log; (c) vertical seismic profiler (VSP) ; and (d) borehole temperature measurements. Note the sharp drop in recorded velocities below the BSR at Site 995 and 997 for VSP. Adapted from (Holbrook, 2001; Paull & Matsumoto, 2000).

The deposition in this area is dominated by hemipelagic accumulations of biogenic and terrigenous sediment that is modified and reworked by contour currents associated with the WBUC (Paull et al., 1996a). The high velocity (40 cm s^{-1}) WBUC erodes into the sediments of the Blake Ridge, which in turn will lead to the re-equilibration of the GHSZ in response (Hornbach et al., 2003). In principle the BSR is thus forced downwards due to the cooling of previously gas charged zones that were in the free gas domain now falling within the envelope

158 for hydrate formation. As a result, reflectors bearing the hallmarks of hydrate related BSRs such
159 as opposite seismic polarity to the seabed can be found at depths well within the accepted GHSZ.
160 These have variously been referred to as palaeo-BSRs in the literature.

161 The indicators for the existence of a hydrate and free gas multi-phase model arose from
162 discrepancies between previously modelled predictions of hydrate concentrations and the results
163 of chemical profiles (Burwicz & Rüpke, 2019). Estimates of hydrate concentration vary between
164 2 – 7% (Egeberg & Dickens, 1999; Paull et al., 1996a; Wood & Ruppel, 2000). The multi-phase
165 component simply proposes the existence of both frozen hydrate and free gas together at the
166 GHSZ (Paganoni et al., 2018).

167 ## 2 Materials and Methods

168 The subsurface thermal modelling workflow is underpinned by the use of seismic data. A
169 key component of the workflow is the presence of an identifiable BSR on seismic reflection data
170 to help derive a proxy for shallow heat flow. This workflow has been applied in this area with
171 some modifications (Fig. 4) through the use of one-dimensional models of subsurface
172 temperature corresponding to existing ODP sites.

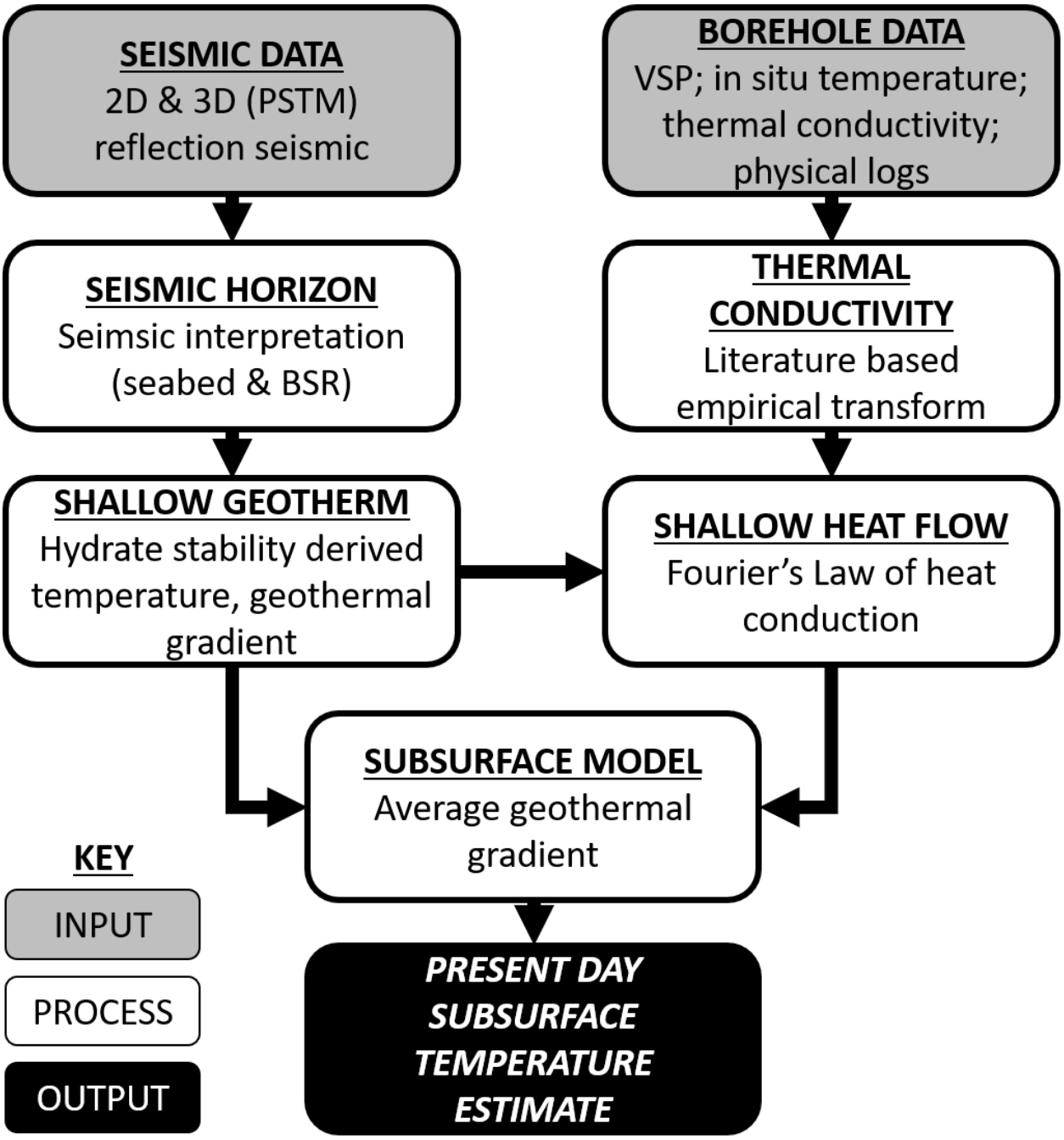

Figure 4. Reflection seismic thermometry process utilized in this study for estimating subsurface temperature.

2.1 Shallow thermal regime

Previous literature has demonstrated the use of mapping BSRs at the base of gas hydrate stability to mark an isotherm (Calvès et al., 2010; Serié et al., 2017; Vargas-Cordero et al., 2010). Hydrate stability is primarily controlled by pressure and temperature, and to a lesser extent other factors such as salinity of the pore fluid or the composition of trapped gases (Dickens & Quinby-Hunt, 1994; Sloan et al., 1998). Gas hydrates in the Blake Ridge have been extensively studied and as such their geochemical parameters are well constrained (Egeberg & Dickens, 1999). By identifying the BSR on seismic reflection data, assuming that it marks the base of the GHSZ, application of a suitable hydrate stability phase model can enable the derivation of temperature at this depth. The seismic reflection volume is in the time domain, thus depth conversion of the two-way travel time (TWT) seismic horizons must be completed. This is to determine both temperature and pressure conditions at the sediment water interface and the phase boundary. Extensive velocity analyses of the Blake Ridge subsurface have revealed that the seabed velocities are low (~ 1400 m s^{-1}) and these low velocities are likely not artefacts (Hornbach et al., 2003). A constant velocity (of 1480 m s^{-1}) has been utilized for the depth conversion of the seabed. In the absence of a detailed velocity model, VSP velocities (Fig. 3c) from the nearby ODP sites are averaged over the interval depths corresponding to the recorded GHSZ. This is done in order to maintain consistency with the use of these velocities at a later stage to derive thermal conductivity variability with depth. An isopach map in TWT of the GHSZ thickness is created. Using the interval velocity averaged over the GHSZ (1688 m s^{-1}), the isopach map is converted to represent a depth thickness to which the seabed depth for each point in XY coordinate space are convolved. In doing so a BSR depth map is produced, which combined with our seabed depth map are the two primary deliverables from seismic interpretation that are necessary for the subsequent thermal regime modelling.

As stated earlier the conditions for hydrate stability must be defined. Key parameters include the trapped gas composition and fluid salinity. Most of the recovered cores from Sites 994, 995 & 997 are noted as being gassy, with reports noting significant degassing of some sections (Paull et al., 1996b). The released gas is mostly methane with minor quantities of CO_2. This is supported by gas samples taken from piston core samples which show a primarily methane hydrate with up to 98% methane, ~1% CO_2 and negligible amounts of ethane and propane from total volumes exceeding 350 mL (Paull et al., 1996b,c). Chemical analyses of water samples from pressure core samplers (PCS) at Site 995 for example yield an average

salinity of 33.3 g kg^{-1} (Paull et al., 1996c). Interstitial water chemistry yields an identical average salinity, consistent with the assumption made for modelling. Site 997 also has very similar interstitial water chemistry to Sites 994 and 995 (Paull et al., 1996d). A later ODP Leg 172 targeting the nearby area also recorded salinity records consistent to an average salinity of 33.3 g kg^{-1} (Keigwin et al., 1998).

With trapped gas composition and fluid salinity established, a suitable model for the hydrate stability field must be utilized. Two such models are utilized, based on the experimental work of Dickens & Quinby-Hunt (1994); and Lu & Sultan (2008), referred to as Model 1 and Model 2 respectively. Dickens & Quinby-Hunt's hydrate stability relationship (Equation 1) is adapted for temperature at the phase boundary.

Equation 1: $$T_{BSR} = ((3.79 \times 10^{-3} - 2.83 \times 10^{-4}(\log(\rho \times g \times Z_{BSR})))^{-1}) - 273$$

Where T_{BSR} is the temperature at GHSZ (°C); ρ is density (kg m^{-3}) (of seawater); g is acceleration due to gravity (m s^{-2}) and Z_{BSR} is the depth (m) of the BSR.

Similarly Lu & Sultan's relationship (Equation 2) is adapted to give temperature at the phase boundary in degree Celsius instead of Kelvin as in the original equation.

Equation 2: $$T_{BSR} = \frac{(\ln P - \ln F_S - E_S S)}{C_S S + D_S} - 273$$

Where T_{BSR} is temperature at the BSR (°C); P is pore fluid pressure (MPa); S is salinity; F_s, C_s, D_s & E_s are empirical constants.

F_s = 1.010769956 * 10^{-9}; C_s = 0.1711726397; D_s = 0.1046133676; E_s = -34.14836102

Both hydrate stability modelling scenarios are made assuming pure methane as the trapped gas and seawater as the interstitial fluid with a salinity of 3.35%. A hydrostatic fluid pressure gradient is also assumed for the modelling scenarios. Water density ρ_w of 1054.6 kg m^{-3} is based on pressure data from ODP records, and is consistent with density expected for deep water in the North Atlantic (Wang et al., 2010). ODP records also indicate that pore pressures, particularly at the crest of the ridge were marginally (up to 0.000526 MPa m^{-1}) above hydrostatic pressure (Paull et al., 1996d). Fluid overpressure is to be expected near the crest of the ridge, as fluids can be expected to migrate up from the flanks, which are expected to be under-pressured. The degree of overpressure increases from Site 994 to Site 997 in accordance with the increasing

proximity to the ridge crest (Paull et al., 1996b, 1996c, 1996d). Studies of the elastic properties of uncompacted and overpressured sediments show that for this degree of fluid overpressure, acoustic velocities will increase by a negligible amount (~2 – 4 %) (Lee, 2003). Furthermore ODP thermal conductivity data was corrected to seafloor temperature and hydrostatic pressure conditions (Ratcliffe, 1960). Having the BSR mapped in the depth domain enables the calculation of hydrostatic pressure at this depth.

Bottom water temperature (BWT) or the temperature at the sediment water interface (SWIT) can be acquired from open source literature such as the National Oceanic and Atmospheric Administration (NOAA) World Ocean Atlas (WOA) (Boyer et al., 2005; Locarnini et al., 2013). These are annualised mean data points for water column temperatures at standard depth intervals as defined by NOAA, at either 0.25° or 1°grid resolution. During the 1D modelling of pseudo boreholes corresponding to existing ODP sites 994, 995 and 997, the WOA temperature record from the nearest geographic grid node did not extend deep enough to the seabed in these locations. Instead seabed temperature was interpolated by synthetically modelling the hydrothermal gradient. This assigns simple regression fit to raw WOA data corresponding to three main pelagic subdivisions of the water column (Sarkar, 2020).

Equation 3:

$$T_{SEABED} = (0.0001 * Z^2) - 0.038 * Z + 22.923 \quad \text{if } Z \leq 200$$

$$T_{SEABED} = (0.00000003 * Z^3) - (0.00007 * Z^2) + 0.0318 * Z + 14.863 \quad \text{if } 200 < Z < 1000$$

$$T_{SEABED} = 1423.4 * Z^{-0.791} \quad \text{if } Z \geq 1000$$

where T_{SEABED} is the modelled hydrothermal gradient temperature (°C) and Z is seabed depth (m).

If temperature at seabed is known, a simple linear geothermal gradient can be established using the following relationship.

Equation 4:

$$\frac{dT}{dZ} GHSZ = \frac{T_{BSR} - T_{SEABED}}{Z_{BSR} - Z_{SEABED}}$$

Where dT/dZ is geothermal gradient (°C km^{-1}); T_{BSR} is temperature at BSR (°C); T_{SEABED} is seabed temperature (°C); Z_{BSR} is depth of BSR (km); Z_{SEABED} is seafloor depth (km).

2.2 1D modelling of boreholes

The BSR derived shallow geothermal gradient may be compared to published geothermal gradients in the ODP record. Basin modellers may use this derived geothermal gradient to inform their 1D or 2D models. For this study, the nearby ODP boreholes will form the basis for 1D models corresponding to each site. Creating these models is necessary as the borehole locations lie outside the extent of the 3D seismic reflection data (Fig. 1b). To model the thermal profile for each borehole, further information about the subsurface thermal regime such as thermal conductivity and heat flow are needed. If we assume a constant thermal conductivity over a range of depths with corresponding temperature measurements, and that heat transfer is solely vertical and occurs through conduction only, it becomes possible to calculate heat flow using the 1D steady state approximation of Fourier's Law as shown in Equation 5.

Equation 5: $$Q = k \times \frac{dT}{dZ}$$

Where Q is heat flow (mW m^{-2}); k is thermal conductivity (W m^{-1} K^{-1}) and dT/dZ is geothermal gradient (°C km^{-1}).

Heat flow probe data is rare and published heat flow information is usually derived from boreholes using thermal conductivity and geothermal gradient. Thermal conductivity is a measure of how well heat is conducted through a material (Popov et al., 2003). Thermal conductivity probe data is difficult to gather, suffering from contact issues between the measurement tool and borehole wall (Brigaud et al., 1990; Nole et al., 2017). There has been extensive study into deriving thermal conductivity from other physical parameters such as velocity measurements for example (Esteban et al., 2015; Leadholm et al., 1985; Pimienta et al., 2018; Rosenbaum et al., 2007). Thermal conductivity is found to be sensitive to mineral composition, porosity and the presence of fractures (Gegenhuber & Schoen, 2012; Hartmann et al., 2005). Velocity is also sensitive to these factors. An empirical transformation from velocity to thermal conductivity has been developed (Equation 6) and adapted from existing experimental data for samples covering a wide array of major lithologies. Best fit regressions have been applied through sample points for wet sample points only, in order to best represent the fluid saturation in the subsurface of the study area (Fig. 5). In previous work (Sarkar, 2020) acoustic velocity in the form of seismic processing velocities were used in Equation 6 to derive thermal conductivity. Due to the lack of such seismic processing velocities in this area, borehole velocities from VSP data have been utilized.

295 **Equation 6:** $k_V = 2.1409 \ln V_p - 14.759$

296 Where k_V is thermal conductivity from velocity (W m^{-1} K^{-1}) and V_P is P wave velocity (m
297 s^{-1}).

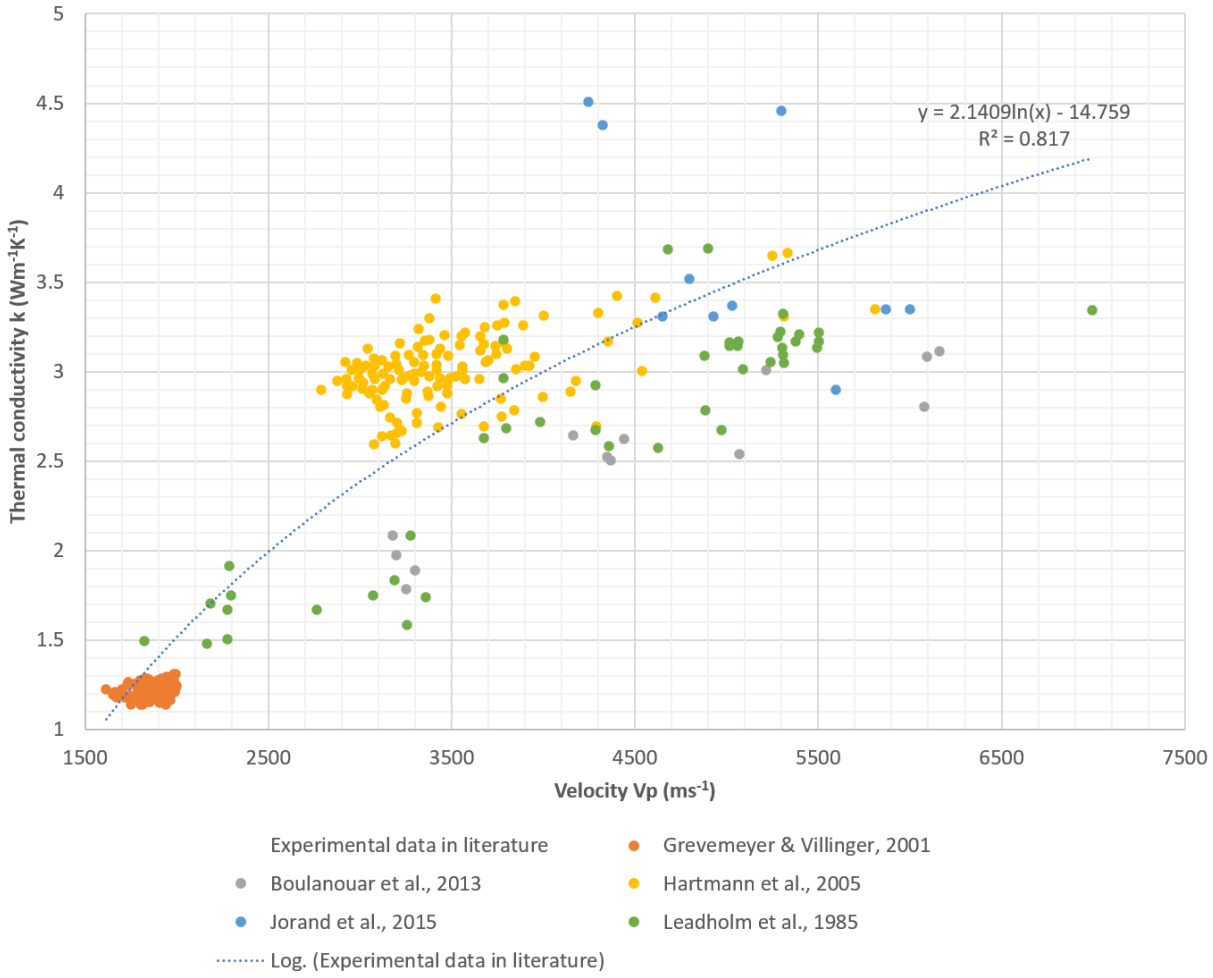

298

299 **Figure 5**. Empirical velocity to thermal conductivity transform utilized in this study. Data shown
300 includes published experimental data for wet samples. Adapted from (Boulanouar et al., 2013;
301 Grevemeyer & Villinger, 2001; Hartmann et al., 2005; Jorand et al., 2015; Leadholm et al.,
302 1985). In previous work (Sarkar, 2020) additional data points were utilized for this empirical
303 transformation containing data from studies such as Mielke et al. (2017). These contained sample
304 data for igneous lithologies for example. Lithological constraint for the target interval for the
305 Blake Ridge is absent such lithologies. Thus, some of those previously used studies were

306 excluded from the point cloud, with the belief that a better fit for the thermal conductivity of the
307 shallow sediments of the Blake Ridge would be determined.

308

309 The shallow geothermal gradient valid for the GHSZ (Equation 4) can be used alongside
310 the derived thermal conductivity (Equation 6) to derive a shallow heat flow proxy for each
311 borehole (using Equation 5). To compute such a heat flow proxy valid for the GHSZ, thermal
312 conductivity in each 1D borehole model is averaged over the GHSZ interval. Calculating such a
313 BSR heat flow proxy has its advantages. A BSR heat flow proxy corresponds to BSR extent on
314 seismic data as opposed to traditional point measurements (Shankar et al., 2014). At this stage
315 each borehole model has an existing synthetic thermal conductivity profile (derived using
316 Equation 6).

317 Temperature below seafloor is a function of depth below the seafloor and the geothermal
318 gradient. Instead of extrapolating the shallow geothermal gradient valid only for the GHSZ, it is
319 possible to use the BSR heat flow proxy and derived thermal conductivity to compute a
320 nonlinear geothermal gradient. It is now possible to use this geothermal gradient to calculate
321 temperature at any given point below the seabed (Equation 7), with the addition of seabed
322 temperature necessary to incorporate the impact of the hydrothermal gradient on the temperature
323 of shallow sediments.

324 **Equation 7:** $$T = T_{SEABED} + (\frac{dT}{dZ} \times Z_{SUBSURFACE})$$

325 where T is predicted temperature (°C); T_{SEABED} is the temperature at seabed (°C)
326 (Equation 4); dT/dZ is the instantaneous geothermal gradient (°C km^{-1}) (Equation 5); and
327 $Z_{SUBSURFACE}$ is the subsurface depth (km).

328 A seismic interpretation suite (Schlumberger Petrel) was used for the seismic
329 interpretation and shallow thermal regime modelling in 3D (Cox et al., 2020; Posamentier,
330 2004). The 1D models were compiled on spreadsheet software (Microsoft Excel).

331 **3 Data**

332 Open source seismic data is used primarily for the estimation of a shallow geothermal
333 gradient and shallow heat flow proxy derived from the BSR. In the absence of seismic velocities,

ODP borehole data acts not only as calibration for the test results but provides a proxy for velocity data.

3.1 Borehole data

Borehole data formed the primary data for this study. The ODP Sites 994, 995 & 997 from Leg 164 investigating the Blake Ridge Hydrate province were chosen (Fig. 1b), particularly due to their proximity (within 10 km) to the available 3D seismic survey (Hornbach et al., 2008; Wood & Ruppel, 2000). The full suite of physical data logs was available from these sites (Fig. 6), of which VSP, thermal conductivity and borehole (in situ-) temperature recordings were of most interest in this study. These measurements extend to hundreds of meters below the seafloor, thus making it suitable as calibration points for the estimation (Fig. 7).

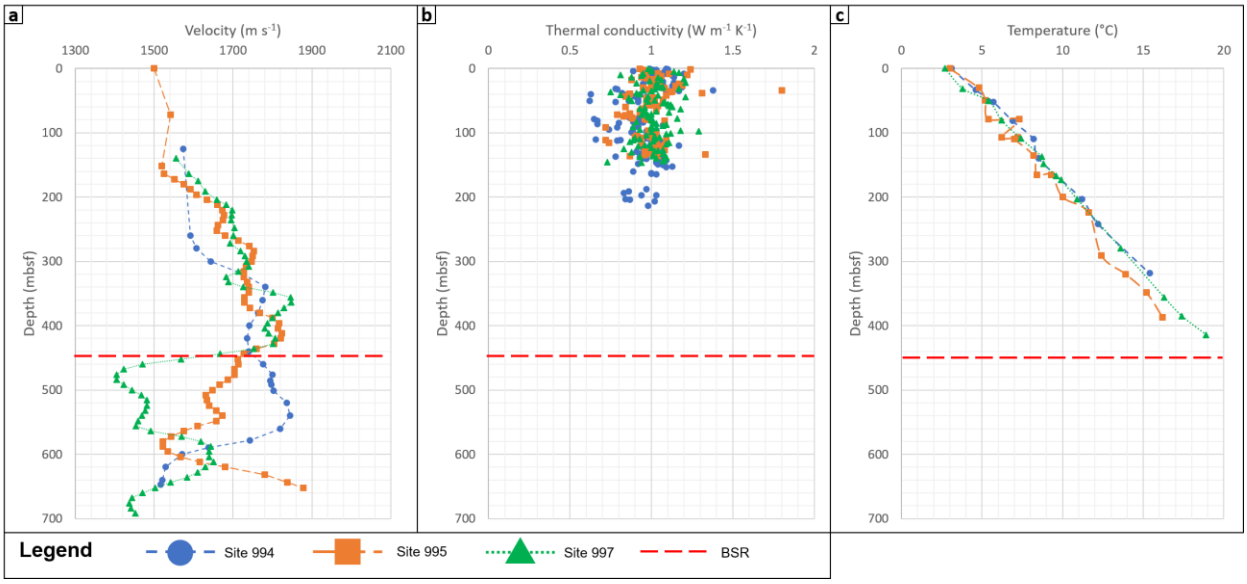

Figure 6. Available data from ODP Leg 164 Sites 994, 995, and 997 plotted for comparison against each other: (a) Velocity data; (b) Thermal conductivity measurements; (c) In situ temperature recordings. BSR depth marked on the basis of average GHSZ thickness across all three sites (see Table 1).

Both zero offset (ZO-) and walkaway (W-) VSP measurements were made using a three component Woods Hole Oceanographic Institution (WHOI) borehole seismometer by the *Cape Hatteras* (Paull et al., 1996b). ZO-VSP data was available for all three sites whereas W-VSP was

available for Sites 994 and 995 only. ZO-VSP was taken at 8 to 10 m intervals returning ~85 traces while W-VSP interval spacing in the hole was ~72 m (Paull et al., 1996a).

Primarily the ZO-VSP helps ascertain free gas presence from the velocity changes below the GHSZ as the down going waves yield the most accurate P-wave interval velocities (Paull et al., 1996a). W-VSP in turn allows the examination of lateral changes in acoustic structure due to the ability to generate both P-waves and converted S-waves, which in turn informs the hydrate development model (Paull et al., 1996a).

ODP in situ temperature measurements are made using a combination of instruments. The two primary instruments used are the Adara and the water-sampling temperature probe (WSTP). A further tool used at the time was the then prototype Davis-Villinger temperature probe (DVTP). These tools are each used in slightly differing circumstances. The Adara APC temperature shoe is used in combination with advanced piston coring (APC) above depths of 170 mbsf. The WSTP and DVTP can be used with an extended core barrel (XCB) and tends to be used for deeper readings. The Adara tool is considered the most reliable in terms of the temperature measurements both due to the greater stability of the data logger and since the readings are calculated from an average of four data records made during firm penetration of the APC tool through hydraulic firing into the sediments (Paull et al., 1996). Measurements made by these other tools require significant corrections to match BWT recorded by the Adara tools (Paull et al., 1996c). When correcting in situ temperature recordings to equilibrium temperature, a shift of ~ 0.3 °C is necessary to account for the discrepancy with the temperature at the mudline. Though statistically only 43% of ODP sites between Legs 101 – 180 with sediment temperature records had reliable temperature measurements, the in situ temperature data at Blake Ridge have been filtered for any erroneous data in order to best calibrate the estimated temperature profiles (Pribnow et al., 2000). Additional thermal data is available from the IHFC database (Gosnold & Panda, 2002).

3.2 Seismic data

This study uses 3D multi-channel, post-stack, time-migrated seismic reflection data from offshore South Carolina (Hornbach et al., 2018). It was acquired to image multiple subsurface geological features (Fig. 2) including the BSR observed at the ridge crest and the more complex

geology on the eastern flank. The survey also targeted part of the eroded sediment wavefield as well as the south east crest of the Blake Ridge itself (Hornbach et al., 2008).

The 3D seismic survey covers an area of 348.93 km^2 and was acquired by the Lamont-Doherty Earth Observatory *R/V Maurice Ewing* in 2000. It is a 40-fold survey with a 2 ms TWT sample rate and grid spacing of 75 m and 37.5 m for inline and crossline respectively. The data was stacked, band pass filtered between 20 to 160 Hz and migrated at a constant velocity (Hornbach et al., 2003). This migration velocity was taken as 1500 m s^{-1}.

Table 1. Combined borehole model input and output table. Thermal modelling input paramteres derived from reported ODP Leg 164 data (Paull & Matsumoto, 2000). Geothermal gradient as reported has been calculated over the depth interval corresponding to the GHSZ in each borehole (an assumed GHSZ thickness is used for Site 994). Heat flow data is from the IHFC. Output results for each borehole are from 1D modelling. Seabed and BSR depth from depth conversion of 3D seismic pick. Temperature at mudline and BSR computed using the seismic pick based depths. Interval velocities are from reported ZO-VSP data for corresponding borehole. Thermal conductivity derived using Equation 6. Average thermal conductivity across all 3 boreholes used to map lateral heat flow variability at BSR depth on seismic (Fig. 7e).

Model	Parameter	Unit	994	995	997	AVERAGE
INPUT	**Seabed**	**m**	2799.1	2778.5	2770.1	
	GHSZ thickness	**m**	429	440	464	444.3333
	ρ_{water}	**kg m^{-3}**	1049.1	1055.9	1058.8	1054.6
	P gradient	**MPa m^{-1}**	0.0106	0.0102	0.00999	0.0103
	Salinity	**%**	3.35	3.35	3.35	
	Velocity (averaged over GHSZ)	**m s^{-1}**	1654	1696	1710	1686.67
	Trapped gas		Methane	Methane	Methane	
	Temperature at BSR	**°C**	n/a	18.7	20	
	Mudline temperature	**°C**	3.1	3	2.7	
	Geothermal gradient	**°C km^{-1}**	35.4	33.5 ± 0.9	36.9 ± 0.4	35.3
	Heat flow	**mW m^2**	35	34	36	35
	Number of calibration points		24	64	67	
OUTPUT	**Seabed**	**m**	2805.47	2782.738	2772.252	
	BSR	**mbsf**	433.5517	434.2092	448.6836	438.81
	Mudline temperature	**°C**	2.671378	2.687033	2.693476	2.68
	Temperature at BSR	**°C**	22.94231	22.90107	22.9019	22.92
	Thermal conductivity derived from velocity	**W m^{-1} K^{-1}**	1.01	1.09	1.08	1.06

	Shallow geothermal gradient	**°C km^{-1}**	46.8	46.6	45	46.13
	Heat flow computed from BSR	**mW m^{2}**	47.1	50.9	48.5	48.83
	Temperature prediction RMSE	**°C**	2.25	2.27	1.23	1.92

4 Results

It is important to note that Sites 994 and 995 are coupled locations (Paull et al., 1996c) and help study profound differences in acoustic responses, manifesting as a BSR or lack thereof, in spite of near identical subsurface geological conditions. Other than a 20 m bathymetric difference, seismic reflection profiles reveal seafloor parallel reflectors with continuous stratigraphy at both sites.

4.1 Sensitivity analyses

The BSR at Blake Ridge has been extensively studied and reported. Therefore, the reported values for GHSZ thickness and BSR depth from ODP records (Table 1) have been used in this study to calibrate the mapped BSR using the 3D seismic volume. There is no record of a BSR at Site 994 although geochemical evidence indicates hydrate presence. Thus the depth of the BSR at this location has been estimated using the trend of the BSR in corresponding sites (Holbrook, 2001). Two primary modelling scenarios were conducted on the basis of experimentally derived hydrate stability fields. To determine which model is most suitable for use at the Blake Ridge, the estimated temperatures were compared to the in situ temperature records for each ODP site, using the same input parameters for salinity; trapped gas composition; and pressure gradient (Table 1). The model with the least divergence from the reported values was deemed to be the desired hydrate stability phase model to use for the workflow. Model 1 had a divergence of 18.2% (averaged between all sites) from reported in situ temperature, whereas Model 2 had an average divergence of 13.9%. Thus Model 2 was deemed to be best representative for the hydrate stability field. To investigate the impact of the different modelling approaches further, the sensitivity of each modelled output was tested and compared between the two approaches. Modelled parameters are overestimated using Model 1, with similar sensitivity between modelled ODP sites. Between sites, the percentage difference varies by 0.01 – 0.02% for BSR temperature, shallow geothermal gradient and BSR derived heat flow proxy.

Additionally, the shallow geothermal gradient and BSR derived heat flow have the same sensitivity. This is to be expected given the direct proportionality as shown in Fourier's Law (Equation 5). The greatest variation is only for the final temperature estimation for Site 994. This may be a consequence of the along trend extrapolation method to determine an estimated position of a BSR in this location, and the fact that Site 994 had fewer than half the calibration points over which the discrepancy percentage amounts were averaged.

4.2 Thermal modelling results contrasted: 1D & 3D modelling approaches

Modelling the thermal regime in 3D using seismic data allows lateral variability (Fig. 7) to be examined compared to the 1D modelling approach conducted for the ODP Sites. The depth domain converted seabed was calibrated against GEBCO bathymetric data (Becker et al., 2009) at 200 m contour intervals. The domain conversion was found to be on average 1.06% shallower compared to the GEBCO bathymetry. The erosional scouring at the seabed visible in the west (Fig. 7a) is in concordance with the eroded sediment wavefield noted in previous studies (Hornbach et al., 2008).

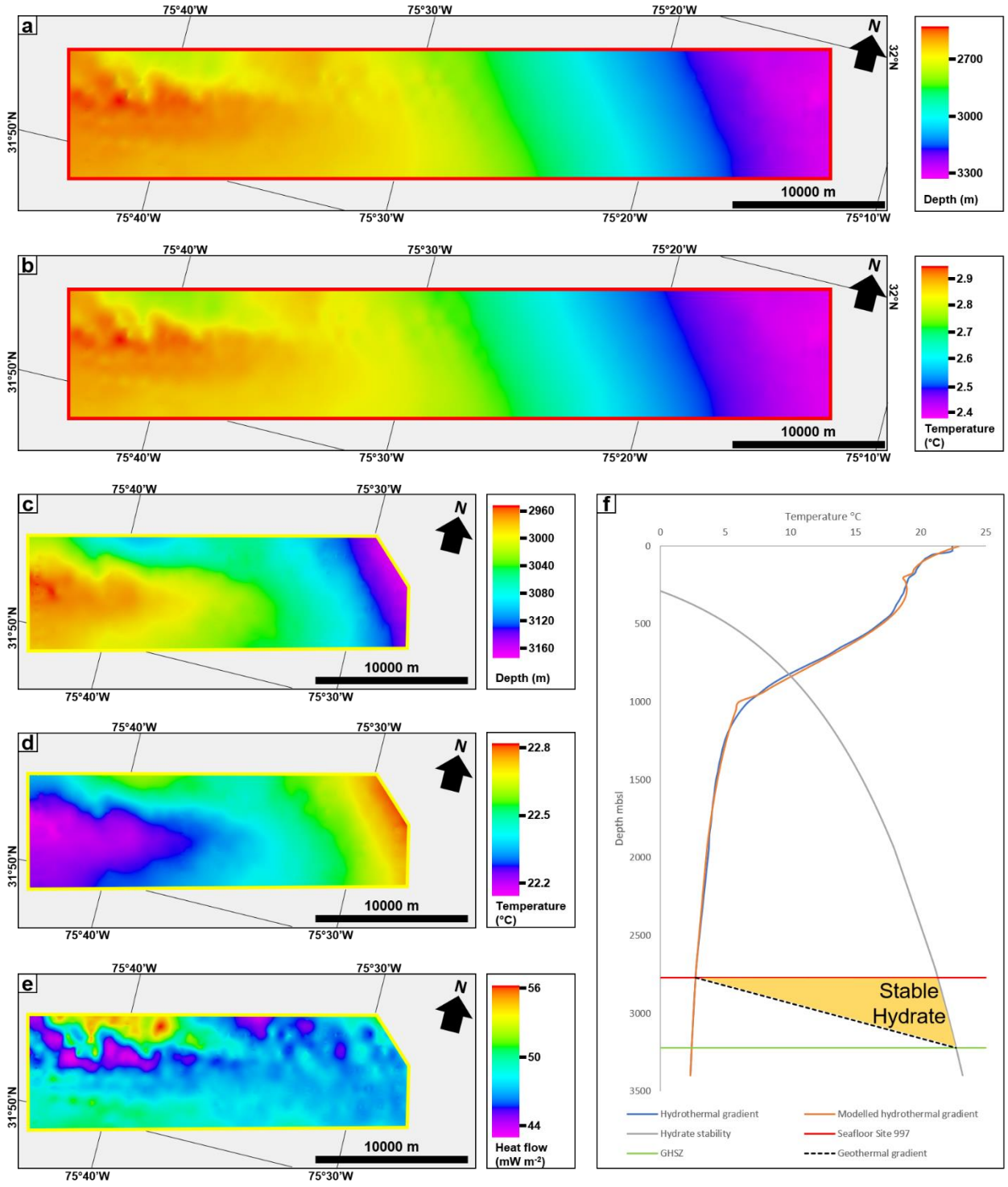

Figure 7. Subsurface seismic interpretation and thermal modelling results. (a) Seabed depth map with visible erosional scouring in NW corner. (b) Seabed temperature map with temperatures modelled from NOAA WOA data as shown from the modelled hydrothermal gradient (see (f)).

443 (c) BSR depth map. (d) Temperature at the base of the GHSZ as defined by the hydrate stability
444 field. (e) Shallow heat flow estimated using BSR derived shallow geothermal gradient and
445 thermal conductivity averaged across the GHSZ. (f) Hydrate stability modelled at ODP Site 997
446 for a pure methane saltwater mixture displayed with the modelled hydrothermal gradient
447 (Dickens & Quinby-Hunt, 1994; Lu & Sultan, 2008). As WOA recordings from the nearest
448 measurement node do not extend deep enough to reach seabed at Site 997, a synthetic
449 hydrothermal gradient is used to extrapolate.

450

451 Temperatures at the seabed (SWIT) modelled using WOA data (Fig. 7b) are an average
452 of 8.15% lower than mudline temperatures reported from borehole temperature measurements.
453 The magnitude of misfit in this input parameter for the modelling is similar to other modelled
454 parameters (see Section 4.1).

455 BSR depth ranges between 2952 – 3172 mbsf with corresponding pressures of 29.8 –
456 32.0 MPa of hydrostatic pressure head. Using Model 2 (Equation 2), BSR temperature modelled
457 over 3D seismic ranges between 21.2 – 22.8 °C with an average temperature of 22.4 °C . The
458 coolest regions of the BSR (Fig. 7d) correspond with the shallowest depth for the base of GHSZ
459 (Fig. 7c) as would be expected from the hydrate stability field curve (Fig. 7f). Results of the 1D
460 model are compared to the reported ODP data for Sites 995 and 997 (Table 1). BSR temperature
461 is warmer using the 1D modelling approach versus from ODP records (Paull et al., 1996).

462 The shallow geothermal gradient computed using the BSR (Equation 3) can be compared
463 against the results reported within the ODP report (Table 1). The BSR derived geothermal
464 gradient is on average 10.9 °C km^{-1} higher than the value reported by the ODP though it must be
465 noted that the ODP results are not reported over the full extent of the corresponding GHSZ and
466 that this might result in some of the discrepancy.

467 The modelled heat flow ranges between 42.9 – 56.2 mW m^{-2} with an average of 47.8 mW
468 m^{-2} and has been computed at the base of GHSZ to demonstrate the lateral variability within the
469 extent of the 3D seismic reflection data. The pockmarked variations in heat flow (Fig. 7e) can be
470 directly attributed to variations in geothermal gradient at the same positions. The pattern of this
471 variability corresponds with bathymetric variations resulting from features such as the erosional
472 scouring (Fig. 2a). The greater seabed depth at the erosional scouring implies cooler seabed

473 temperatures at these locations. Though BSRs mimic seafloor morphology, the rapid rate of
474 erosion due to the WBUC would not allow the observed seismic marker, that is, the phase
475 boundary of gas hydrates to re-equilibrate quickly enough. Thus, the BSR below the erosional
476 scours will not be proportionately deeper and as a result the GHSZ is thinner in this location. As
477 a consequence, the shallow geothermal gradient (Equation 4) will be higher in this region, which
478 using Fourier's Law (Equation 5) directly translates to the higher heat flows observed. Similarly,
479 regions of raised relief are marked by low heat flow (Fig. 7e) as the computed shallow
480 geothermal gradient will be lower. Heat flow modelled at point locations during the 1D
481 modelling (Table 1), although outside the extent of the 3D seismic reflection data, all lie within
482 one standard deviation of the mean heat flow. Heat flow modelled at Site 997 is closest to the
483 average heat flow modelled from seismic data (0.41% lower). It is possible the proximity of this
484 site to the edge of the extent of the seismic data (Fig. 1a) contributes to this. On average, heat
485 flow modelled at ODP sites are 0.51% higher than the average reported from the estimation
486 using the BSR. Therefore, heat flow modelled at point locations or using seismic data will
487 produce consistent results.

488 On average the subsurface temperature predicted using the presented methodology is
489 found to be an average of 1.53 °C higher than the in-situ temperature readings for each site (Fig.
490 8).

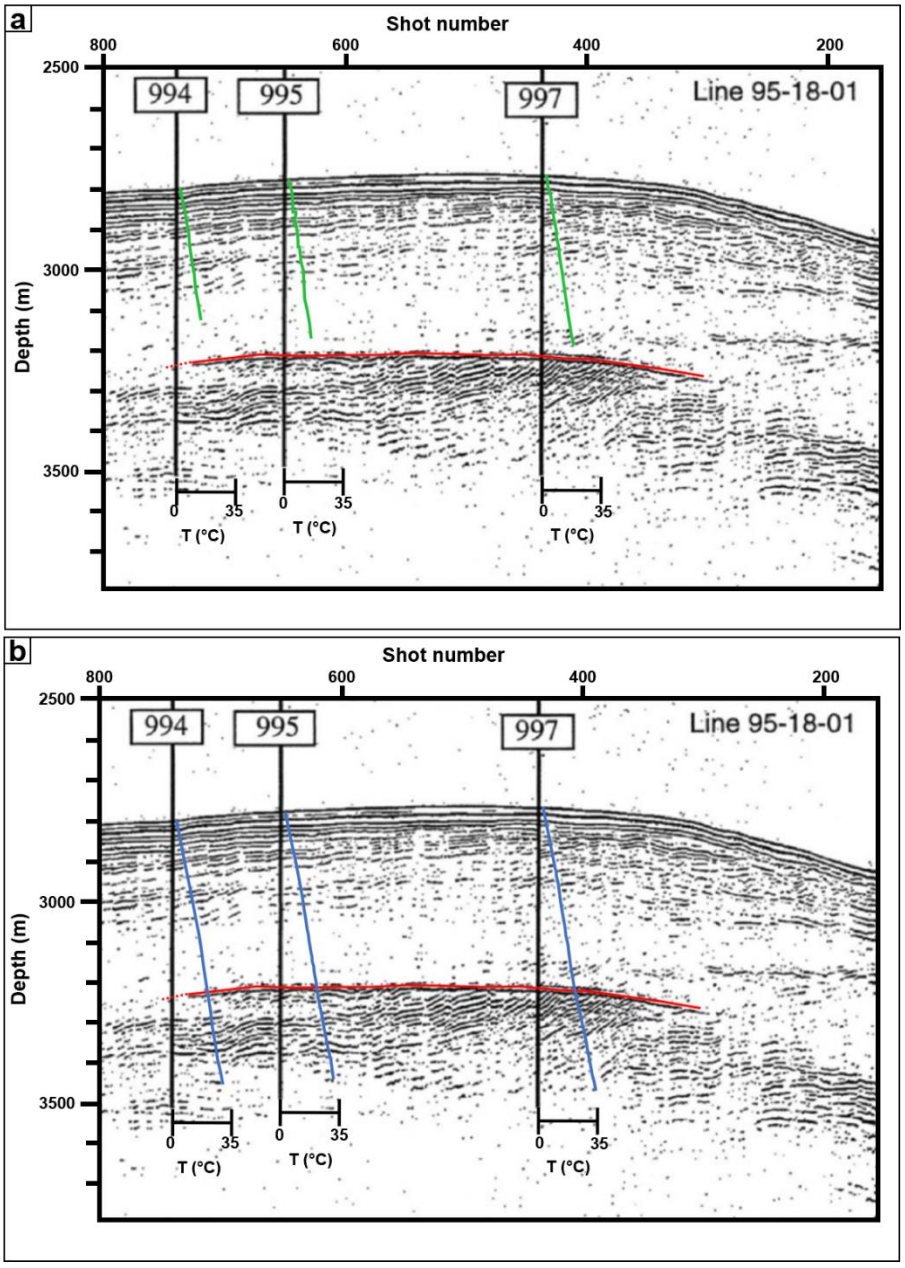

Figure 8. (a) Existing subsurface temperature profile from ODP data for Blake Ridge; (b) Subsurface temperature profile estimated using the seismic workflow. Temperatures are calculated from the velocities not only down to the interface at the base of the GHSZ marked by the BSR, but also ~200 m below it.

The estimated temperature profiles closely follow the trend of the measured data (Fig. 9). Sporadic negative temperature excursions are observed such as at ~340 mbsf at Site 997. Low

499 temperature thermal anomalies in hydrate bearing sediment can be attributed to the hydrate
500 dissociation process, which is endothermic in nature (Sloan, 1990). Negative temperature
501 excursions shown in the predicted temperature profiles (particularly Sites 995 and 997) are
502 observed at depths consistent with the thermodynamic base of the GHSZ (reported to extend
503 down to ~540 mbsf). These temperature excursions would appear to support the hypothesis of
504 hydrate existing in a multi-phase system comprising frozen hydrate and dissociated free gas
505 down to the thermodynamic base of the GHSZ. It must also be noted that any trends in the
506 velocity profile can be expected to translate through the modelling workflow to the final
507 temperature output. The excursions in the temperature signal could be an artefact of a velocity
508 change recorded by the borehole seismometer. Equally if a lithological interface causes the
509 velocity response, it can be expected that the contrast in thermal properties across this interface
510 would have a corresponding temperature contrast.

511 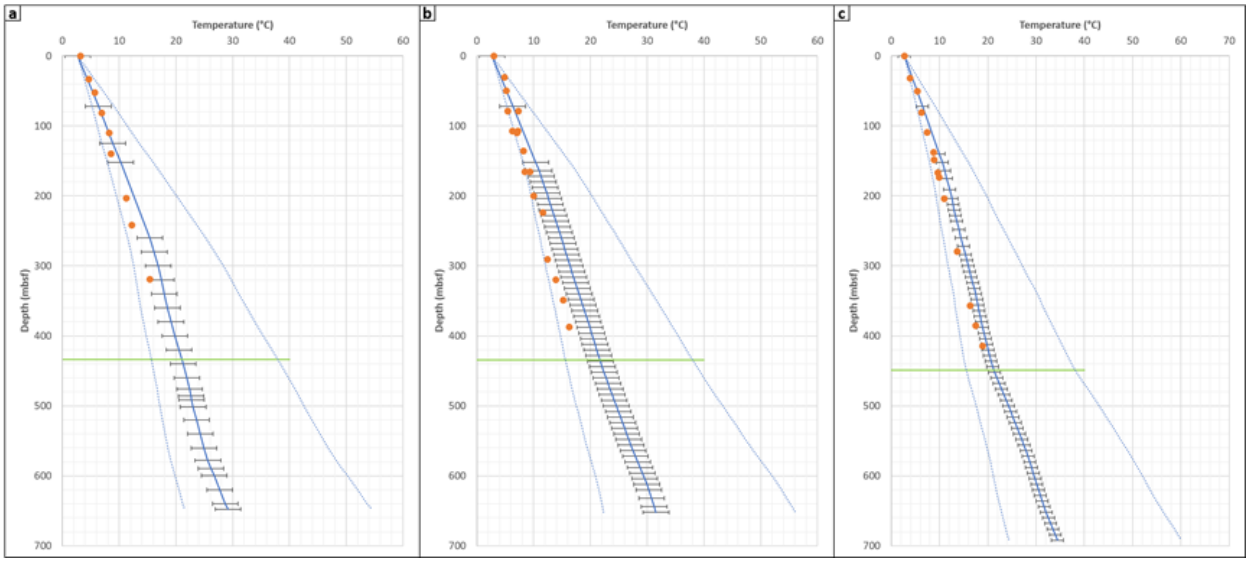

512 **Figure 9**. Predicted temperature profiles (solid blue line) for Sites 994 (a); 995 (b), and 997 (c),
513 using the reflection seismic thermometry workflow discussed against the reported borehole in
514 situ temperature recordings (orange points). BSR depth at each location is shown for reference
515 (solid green line). 95% confidence interval bounds representing the outer limits of predicted
516 results are also shown (dotted blue line). Error bars are based on root mean squared error
517 (RSME) at each site (Table 1). Due to the VSP record not going to mudline at Sites 994 and 997,
518 velocity readings from Site 995 were substituted for this missing interval. Average discrepancies

519 in measurements are 11.5%, 16.4% and 10.8% respectively over the corresponding temperature
520 range, with a combined average of 12.9% higher than the borehole temperature readings.

521

522 **5 Discussion**

523 In a predictive workflow reliant on multiple parameters, uncertainty in the final derived
524 property can become compounded. In order to determine the range within which the predicted
525 properties vary, they are modelled using upper and lower bounds corresponding to 95% of all
526 values. In this manner it was possible to determine the upper and lower bound for the heat flow
527 derived from BSR (interpreted on the 3D seismic volume). Determining this heat flow bound
528 (using Equation 5) required the upper and lower bound for interval velocity within the GHSZ
529 and the corresponding thermal conductivity to be known. Shallow geothermal gradient is
530 considered unchanged as the variability in the seafloor depth and BSR depth is considered
531 negligible, and since the composition of the hydrate in this area is well known, the temperature at
532 BSR will not vary greatly. Heat flow ranges between 35.7 – 73.5 mW m^{-2}. This range is
533 consistent with reported IHFC results in the study area (Pribnow et al., 2000). When applying the
534 same 95% confidence interval technique to establish a range within which the temperature
535 predictions will lie, it becomes apparent the upper bound is considerably higher (Fig. 9). The
536 lower bound roughly lies within one standard deviation of the mean case thermal profile. When
537 tracing the sensitivity of the upper bound it is found that the regression representing thermal
538 conductivity from velocity is the source of this great variability. Velocities in the GHSZ in this
539 area when plotted against Fig. 5 would all cluster around the lowest end of the point cloud. When
540 computing the 95% confidence interval bounds for the whole array of points, the regression will
541 include much higher velocities and correspondingly much higher thermal conductivity as the
542 upper bound. This is what leads to the much higher upper bound seen in Fig. 9. If focusing only
543 on those experimental data points corresponding to the velocities within the GHSZ (Grevemeyer
544 & Villinger, 2001), it is not possible to derive a statistically valid regression ($R^2 << 0.1$). Thus, it
545 must be noted that though the range of possible temperature predictions using the regression
546 from Fig. 5 (Equation 6) is large, it still provides the best possible means of deriving a first pass
547 approximation that fits well to recorded data. RMSE has been used as a measure of accuracy to

compare forecasting errors in predicted temperature against the reported data from ODP studies (Barnston, 1992). Results from the model have an RMSE between 1.23 – 2.27 °C (Table 1).

A significant caveat remains the sensitivity of acoustic velocity. A direct relationship (Equation 6) has been made between velocity and thermal conductivity but such a relationship becomes compromised if velocity is independently affected by another factor. This may be the impact of fluid over-pressure on recorded velocities or it could be the impact of mineral layering within the rock column on thermal conductivity. Another assumption made is the dominance of heat transport through conduction in the area, thus enabling the use of Fourier's Law to underpin the thermal modelling work. The modelling results from this dataset have not demonstrated an impact from any of the above factors, though it provides an opportunity for further investigation using a dataset that allows for the impact of these factors on the modelling workflow to be explored. The data rich North Sea Basin would prove an excellent setting for such a study and this has been explored in (Sarkar, 2020).

Characterising subsurface thermal regime using 3D seismic data presents an opportunity to examine the lateral variability in thermal properties not hitherto possible with point data. This is best demonstrated in Fig. 7e where the heat flow variability is mapped on the GHSZ interface. These lateral variations can further be tied to the topographic variability at the sediment interface, indicating the manner in which structural and bathymetric features may impact the transfer of heat in the shallow subsurface. This data can then be viewed in real time on seismic interpretation software. The scale at which the variability in heat flow can be discerned in this manner is far smaller than the magnitude larger scale of available heat flow maps in the literature. Furthermore, with the greater extent of modern-day seismic coverage in comparison to point heat flow data, it may become possible to fill in gaps in lateral coverage.

Modelling thermal regime in this manner not only extends laterally but vertically too. The 1D modelling methodology also produced subsurface thermal models. Only 53 ODP legs between Leg 101 – 180 had temperature data of which only 43% is considered reliable (Pribnow et al., 2000). While it is not known how many of these sites also encountered gas hydrates, the standard logging suite of ODP data should be available for these. The 1D modelling approach utilised this ODP data. For continental margin ODP sites that display either geophysical or geochemical indications of gas hydrate presence, the methodology presented in this paper

introduces a process for deriving reliable subsurface thermal data for such sites with extensive seismic data coverage that may lack published thermal data. Crucially, these temperature models extend the understanding of the thermal regime a further 260 – 330 m beyond existing data ODP thermal data. This would provide a means to expand the global database for subsurface thermal data, with the ancillary benefits to understanding in different domains that would be a natural corollary.

6 Conclusions

This study shows the results of a reflection seismic thermometry methodology underpinned by seismic data from the Blake Ridge offshore east coast USA. It was able to take open source 3D seismic data to map a BSR and derive lateral heat flow variability across the crest of the ridge structure, and image the impact of erosional scouring on the seabed on heat flow in the shallow subsurface. The methodology was also able to predict and extend the subsurface temperature record beyond the record available from nearby ODP boreholes. This predicted thermal profile now extended through the GHSZ and into the underlying gas charged sediment. Calibrating the temperature predicted in this manner against ODP records determines that reliable first pass estimates can be derived in deep water passive margin settings where seismic data is available, but borehole data is lacking. This would be a powerful tool for geoscientists to not only further their understanding of subsurface petroleum systems but can be utilised for geothermal energy applications and monitoring the impact of temperature on subsurface microbial communities. It is envisaged that reflection seismic thermometry may be applied to other such deep-water passive margin basins.

Acknowledgments, Samples, and Data

All data are publically available from corresponding data repositories listed in the methods section. Data interpretation was performed using the Petrel suite software donated from Schlumberger. ADS is supported by funding from his parents. Special thanks go to Kofi Owusu for his comments and assistance. Thanks also go to David Cox & Conor O'Sullivan for their insightful comments.

References

Barnston, A. G. (1992). Correspondence among the correlation, RMSE, and Heidke forecast verification measures; refinement of the Heidke score. *Weather and Forecasting*, *7*(4), 699–709. https://doi.org/10.1175/1520-0434

Becker, J. J., Sandwell, D. T., Smith, W. H. F., Braud, J., Binder, B., Depner, J., Fabre, D., Factor, J., Ingalls, S., Kim, S.-H., Ladner, R., Marks, K., Nelson, S., Pharaoh, A., Trimmer, R., Von Rosenberg, J., Wallace, G., & Weatherall, P. (2009). Global Bathymetry and Elevation Data at 30 Arc Seconds Resolution: SRTM30_PLUS. *Marine Geodesy*, *32*(4), 355–371. https://doi.org/10.1080/01490410903297766

Bonté, D., Van Wees, J. D., & Verweij, J. M. (2012). Subsurface temperature of the onshore Netherlands: New temperature dataset and modelling. *Geologie En Mijnbouw/Netherlands Journal of Geosciences*, *91*(4), 491–515. https://doi.org/10.1017/S0016774600000354

Boulanouar, A., Rahmouni, A., Boukalouch, M., Samaouali, A., Géraud, Y., Harnafi, M., & Sebbani, J. (2013). Determination of Thermal Conductivity and Porosity of Building Stone from Ultrasonic Velocity Measurements. *Geomaterials*, *03*(04), 138–144. https://doi.org/10.4236/gm.2013.34018

Boyer, T., Levitus, S., Garcia, H., Locarnini, R. A., Stephens, C., & Antonov, J. (2005). Objective analyses of annual, seasonal, and monthly temperature and salinity for the World Ocean on a 0.25° grid. *International Journal of Climatology*, *25*(7), 931–945. https://doi.org/10.1002/joc.1173

Brigaud, F., Chapman, D. S., & Le Douaran, S. (1990). Estimating thermal conductivity in sedimentary basins using lithologic data and geophysical well logs. *American Association of Petroleum Geologists Bulletin*, *74*(9), 1459–1477. https://doi.org/10.1306/0C9B2501-1710-11D7-8645000102C1865D

Burwicz, & Rüpke. (2019). Thermal State of the Blake Ridge Gas Hydrate Stability Zone (GHSZ)—Insights on Gas Hydrate Dynamics from a New Multi-Phase Numerical Model. *Energies*, *12*(17), 3403. https://doi.org/10.3390/en12173403

Calvès, G., Huuse, M., Schwab, A., & Clift, P. (2008). Three-dimensional seismic analysis of high-amplitude anomalies in the shallow subsurface of the Northern Indus Fan:

635 Sedimentary and/or fluid origin. *Journal of Geophysical Research*, *113*(B11), B11103.
636 https://doi.org/10.1029/2008JB005666

637 Calvès, G., Schwab, A. M., Huuse, M., Clift, P. D., & Inam, A. (2010). Thermal regime of the
638 northwest Indian rifted margin - Comparison with predictions. *Marine and Petroleum*
639 *Geology*, *27*(5), 1133–1147. https://doi.org/10.1016/j.marpetgeo.2010.02.010

640 Cox, D. R., Newton, A. M. W., & Huuse, M. (2020). An introduction to seismic reflection data:
641 acquisition, processing and interpretation. In N. Scarselli, J. Adam, & D. Chiarella (Eds.),
642 *Regional geology and tectonics: principles of geologic analysis* (pp. 571–603). Elsevier.

643 Dickens, G. R., & Quinby-Hunt, M. S. (1994). Methane hydrate stability in seawater.
644 *Geophysical Research Letters*, *21*(19), 2115–2118. https://doi.org/10.1029/94GL01858

645 Egeberg, P. K., & Dickens, G. R. (1999). Thermodynamic and pore water halogen constraints on
646 gas hydrate distribution at ODP Site 997 (Blake Ridge). *Chemical Geology*, *153*(1–4), 53–
647 79. https://doi.org/10.1016/S0009-2541(98)00152-1

648 Esteban, L., Pimienta, L., Sarout, J., Piane, C. D., Haffen, S., Geraud, Y., & Timms, N. E.
649 (2015). Study cases of thermal conductivity prediction from P-wave velocity and porosity.
650 *Geothermics*, *53*, 255–269. https://doi.org/10.1016/j.geothermics.2014.06.003

651 Fuchs, S., & Balling, N. (2016). Improving the temperature predictions of subsurface thermal
652 models by using high-quality input data. Part 2: A case study from the Danish-German
653 border region. *Geothermics*, *64*, 1–14. https://doi.org/10.1016/j.geothermics.2016.04.004

654 Gardner, J. V. (2013). *Processed Bathymetry Data from the US Atlantic Margin acquired during*
655 *the Ronald H. Brown expedition RB1202*. https://doi.org/10.1594/IEDA/319542

656 Gegenhuber, N., & Schoen, J. (2012). New approaches for the relationship between
657 compressional wave velocity and thermal conductivity. *Journal of Applied Geophysics*, *76*,
658 50–55. https://doi.org/10.1016/j.jappgeo.2011.10.005

659 Gosnold, W., & Panda, B. (2002). *The Global Heat Flow Database of the International Heat*
660 *Flow Commission*. https://doi.org/http://doi.org/10.17616/R3G305

661 Grevemeyer, I., & Villinger, H. (2001). Gas hydrate stability and the assessment of heat flow
662 through continental margins. *Geophysical Journal International*, *145*, 647–660.

https://doi.org/ISI:000169428800007

Haacke, R. R., Westbrook, G. K., & Hyndman, R. D. (2007). Gas hydrate, fluid flow and free gas: Formation of the bottom-simulating reflector. *Earth and Planetary Science Letters*, *261*(3–4), 407–420. https://doi.org/10.1016/j.epsl.2007.07.008

Hartmann, A. Ã., Rath, V., & Clauser, C. (2005). Thermal conductivity from core and well log data. *International Journal of Rock Mechanics and Mining Sciences*, *42*(7-8 SPEC. ISS.), 1042–1055. https://doi.org/10.1016/j.ijrmms.2005.05.015

Holbrook, W. S. (2001). Seismic Studies of the Blake Ridge: Implications for Hydrate Distribution, Methane Expulsion, and Free Gas Dynamics. In C. K. Paull & W. P. Dillon (Eds.), *Natural Gas Hydrates: Occurrence, Distribution, and Detection* (pp. 235–256). https://doi.org/10.1029/GM124p0235

Holbrook, W. S., Hoskins, H., Wood, W. T., Stephen, R. A., & Lizarralde, D. (1996). Methane hydrate and free gas on the Blake Ridge from vertical seismic profiling. *Science*, *273*(5283), 1840–1843. https://doi.org/10.1126/science.273.5283.1840

Hornbach, M. J., Holbrook, W. S., Gorman, A. R., Hackwith, K. L., Lizarralde, D., & Pecher, I. (2003). Direct seismic detection of methane hydrate on the Blake Ridge. *Geophysics*, *68*(1), 92–100. https://doi.org/10.1190/1.1543196

Hornbach, M. J., Holbrook, W. S., Lizarralde, D., Pecher, I., Gorman, A., Saffer, D., & Van Avendonk, H. (2018). *Processed 3D volume of multichannel seismic data on the Blake Ridge, acquired during R/V Maurice Ewing expedition EW0008 (2008) [Data set]*. Interdisciplinary Earth Data Alliance (IEDA). https://doi.org/10.1594/IEDA/500090

Hornbach, M. J., Saffer, D. M., Holbrook, W. S., Van Avendonk, H. J. A., & Gorman, A. R. (2008). Three-dimensional seismic imaging of the Blake Ridge methane hydrate province: Evidence for large, concentrated zones of gas hydrate and morphologically driven advection. *Journal of Geophysical Research*, *113*(B7), B07101. https://doi.org/10.1029/2007JB005392

Hunt, J. M. (1984). Generation and Migration of Light Hydrocarbons. *Science*, *226*(4680), 1265–1270. https://doi.org/10.1126/science.226.4680.1265

Jorand, R., Clauser, C., Marquart, G., & Pechnig, R. (2015). Statistically reliable petrophysical

properties of potential reservoir rocks for geothermal energy use and their relation to lithostratigraphy and rock composition: The NE Rhenish Massif and the Lower Rhine Embayment (Germany). *Geothermics, 53*, 413–428. https://doi.org/10.1016/j.geothermics.2014.08.008

Keigwin, L. D., Rio, D., & Acton, G. D. (1998). Introduction. In L. D. Keigwin, D. Rio, & G. D. Acton (Eds.), *Proceedings of the Ocean Drilling Program 172 Initial Reports* (Vol. 43, Issue 4, pp. 1–26). Ocean Drilling Program. https://doi.org/10.2973/odp.proc.ir.172.101.1998

Kvenvolden, K. A. (1985). Comparison of marine gas hydrates in sediments of an active and passive continental margin. *Marine and Petroleum Geology*, *2*(1), 65–71. https://doi.org/10.1016/0264-8172(85)90049-2

Kvenvolden, K. A., & Lorenson, T. D. (2001). The Global Occurrence of Natural Gas Hydrate. In C.K. Paull & W. P. Dillon (Eds.), *Natural Gas Hydrates: Occurrence, Distribution, and Detection* (Geophys. M, pp. 3–18). AGU. https://doi.org/10.1029/GM124p0003

Leadholm, R. H., Ho, T. T. Y., & Sahai, S. K. (1985). Heat flow, geothermal gradients and maturation modelling on the Norwegian continental shelf using computer methods. In *Petroleum Geochemistry in Exploration of the Norwegian Shelf* (pp. 131–143). Springer Netherlands. https://doi.org/10.1007/978-94-009-4199-1_9

Lee, M. W. (2003). Elastic properties of overpressured and unconsolidated sediments. In *U.S. Geological Survey Bulletin* (Vol. 2214). https://pubs.er.usgs.gov/publication/b2214

Locarnini, R. A., Mishonov, A. V, Antonov, J. I., Boyer, T. P., Garcia, H. E., Baranova, O. K., Zweng, M. M., Paver, C. R., Reagan, J. R., Johnson, D. R., Hamilton, M., & Seidov, D. (2013). *WORLD OCEAN ATLAS 2013: Temperature Volume 1* (Vol. 1, Issue NOAA Atlas NESDID 81). https://doi.org/10.7289/V55X26VD

Lu, Z., & Sultan, N. (2008). Empirical expressions for gas hydrate stability law, its volume fraction and mass-density at temperatures 273.15K to 290.15K. *Geochemical Journal*, *42*(2), 163–175. https://doi.org/10.2343/geochemj.42.163

Lucazeau, F., Brigaud, F., & Bouroullec, J. L. (2004). High-resolution heat flow density in the lower Congo basin. *Geochemistry, Geophysics, Geosystems*, *5*(3), Q03001.

https://doi.org/10.1029/2003GC000644

McConnell, D. R., & Kendall, B. A. (2002). Images of the Base of Gas Hydrate Stability, Northwest Walker Ridge, Gulf of Mexico. *Offshore Technology Conference*. https://doi.org/10.4043/14103-MS

Mielke, P., Bär, K., & Sass, I. (2017). Determining the relationship of thermal conductivity and compressional wave velocity of common rock types as a basis for reservoir characterization. *Journal of Applied Geophysics*, *140*, 135–144. https://doi.org/10.1016/j.jappgeo.2017.04.002

Natural Gas Hydrates: Occurrence, Distribution, and Detection. (2001). In Charles K. Paull & W. P. Dillon (Eds.), *Geophysical Monograph Series* (Vol. 124). American Geophysical Union. https://doi.org/10.1029/GM124

Nole, M., Daigle, H., Cook, A. E., Hillman, J. I. T., & Malinverno, A. (2017). Linking basin-scale and pore-scale gas hydrate distribution patterns in diffusion-dominated marine hydrate systems. *Geochemistry, Geophysics, Geosystems*, *18*(2), 653–675. https://doi.org/10.1002/2016GC006662

Paganoni, M., Cartwright, J. A., Foschi, M., Shipp, C. R., & Van Rensbergen, P. (2018). Relationship between fluid-escape pipes and hydrate distribution in offshore Sabah (NW Borneo). *Marine Geology*, *395*(April 2017), 82–103. https://doi.org/10.1016/j.margeo.2017.09.010

Paganoni, M., Cartwright, J. A., Foschi, M., Shipp, R. C., & Van Rensbergen, P. (2016). Structure II gas hydrates found below the bottom-simulating reflector. *Geophysical Research Letters*, *43*(11), 5696–5706. https://doi.org/10.1002/2016GL069452

Paull, C. K., & Dillon, W. P. (1981). *Appearance and distribution of the gas hydrate reflection in the Blake Ridge region, offshore southeastern United States*. US Geological Survey. https://doi.org/10.3133/mf1252

Paull, C. K., Lorenson, T. D., Borowski, W. S., Ussler, W. I., Olsen, K., & Rodriguez, N. M. (2000). Isotopic composition of CH4, CO2 species, and sedimentary organic matter within samples from the Blake Ridge: gas source implications. In C. K. Paull, R. Matsumoto, P. J. Wallace, & W. P. Dillon (Eds.), *Proceedings of the Ocean Drilling Program, 164 Scientific*

Results (pp. 67–78). Ocean Drilling Program. https://doi.org/10.2973/odp.proc.sr.164.207.2000

Paull, C. K., & Matsumoto, R. (2000). Leg 164 overview. In C. K. Paull, R. Matsumoto, P. J. Wallace, & W. P. Dillon (Eds.), *Proceedings of the Ocean Drilling Program, 164 Scientific Results* (pp. 3–10). Ocean Drilling Program. https://doi.org/10.2973/odp.proc.sr.164.204.2000

Paull, C. K., Matsumoto, R., & Wallace, P. J. (Eds.). (1996a). *Proceedings of the Ocean Drilling Program, 164 Initial Reports* (Vol. 164, Issue 9). Ocean Drilling Program. https://doi.org/10.2973/odp.proc.ir.164.1996

Paull, C. K., Matsumoto, R., & Wallace, P. J. (1996b). Site 994. In C. K. Paull, R. Matsumoto, P. J. Wallace, & W. P. Dillon (Eds.), *Proceedings of the Ocean Drilling Program, 164 Initial Reports* (Vol. 164, pp. 99–174). Ocean Drilling Program. https://doi.org/10.2973/odp.proc.ir.164.107.1996

Paull, C. K., Matsumoto, R., & Wallace, P. J. (1996c). Site 995. In C. K. Paull, R. Matsumoto, P. J. Wallace, & W. P. Dillon (Eds.), *Proceedings of the Ocean Drilling Program, 164 Initial Reports* (Vol. 164, pp. 175–240). Ocean Drilling Program. https://doi.org/10.2973/odp.proc.ir.164.108.1996

Paull, C. K., Matsumoto, R., & Wallace, P. J. (1996d). Site 997. In C. K. Paull, R. Matsumoto, P. J. Wallace, & W. P. Dillon (Eds.), *Proceedings of the Ocean Drilling Program, 164 Initial Reports* (Vol. 164, pp. 277–334). Ocean Drilling Program. https://doi.org/10.2973/odp.proc.ir.164.110.1996

Paull, C. K., Matsumoto, R., Wallace, P. J., Borowski, W. S., Dickens, G. R., Egeberg, P. K., Lorenson, T. D., Collett, T. S., Ruppel, C., & Holbrook, W. S. (1996). Explanatory Notes. In C. K. Paull, R. Matsumoto, P. J. Wallace, & W. P. Dillon (Eds.), *Proceedings of the Ocean Drilling Program, 164 Initial Reports* (Vol. 164, pp. 13–41). Ocean Drilling Program. https://doi.org/10.2973/odp.proc.ir.164.102.1996

Pimienta, L., Klitzsch, N., & Clauser, C. (2018). Comparison of thermal and elastic properties of sandstones: Experiments and theoretical insights. *Geothermics, 76*(June), 60–73. https://doi.org/10.1016/j.geothermics.2018.06.005

779 Popov, Y. A., Pribnow, D. F. C., Sass, J. H., Williams, C. F., & Burkhardt, H. (1999).
780 Characterization of rock thermal conductivity by high-resolution optical scanning.
781 *Geothermics*, *28*(2), 253–276. https://doi.org/10.1016/S0375-6505(99)00007-3

782 Popov, Y., Tertychnyi, V., Romushkevich, R., Korobkov, D., & Pohl, J. (2003). Interrelations
783 Between Thermal Conductivity and Other Physical Properties of Rocks: Experimental Data.
784 *Pure and Applied Geophysics*, *160*(5), 1137–1161. https://doi.org/10.1007/PL00012565

785 Posamentier, H. W. (2004). Seismic Geomorphology: Imaging Elements of Depositional
786 Systems from Shelf to Deep Basin Using 3D Seismic Data: Implications for Exploration
787 and Development. *Geological Society, London, Memoirs*, *29*(1), 11–24.
788 https://doi.org/10.1144/GSL.MEM.2004.029.01.02

789 Pribnow, D. F. C., Kinoshita, M., & Stein, C. . (2000). Thermal data collection and heat flow
790 recalculations for ODP Legs 101-180. In *Institute for Joint Geoscientific Research*.
791 http://www-odp.tamu.edu/publications/heatflow/

792 Purkamo, L., Kietäväinen, R., Nuppunen-Puputti, M., Bomberg, M., & Cousins, C. (2020).
793 Ultradeep Microbial Communities at 4.4 km within Crystalline Bedrock: Implications for
794 Habitability in a Planetary Context. *Life*, *10*(1), 2. https://doi.org/10.3390/life10010002

795 Ratcliffe, E. H. (1960). The thermal conductivities of ocean sediments. *Journal of Geophysical*
796 *Research*, *65*(5), 1535–1541. https://doi.org/10.1029/JZ065i005p01535

797 Rosenbaum, E. J., English, N. J., Johnson, J. K., Shaw, D. W., & Warzinski, R. P. (2007).
798 Thermal conductivity of methane hydrate from experiment and molecular simulation.
799 *Journal of Physical Chemistry B*, *111*(46), 13194–13205. https://doi.org/10.1021/jp074419o

800 Ruppel, C. D., & Kessler, J. D. (2017). The interaction of climate change and methane hydrates.
801 *Reviews of Geophysics*, *55*(1), 126–168. https://doi.org/10.1002/2016RG000534

802 Ryan, W. B. F., Carbotte, S. M., Coplan, J. O., O'Hara, S., Melkonian, A., Arko, R., Weissel, R.
803 A., Ferrini, V., Goodwillie, A., Nitsche, F., Bonczkowski, J., & Zemsky, R. (2009). Global
804 Multi-Resolution Topography synthesis. *Geochemistry, Geophysics, Geosystems*, *10*(3),
805 Q03014. https://doi.org/10.1029/2008GC002332

806 Sarkar, A. D. (2020). *Reflection Seismic Thermometry*. University of Manchester.

807 Sassen, R., & MacDonald, I. R. (1994). Evidence of structure H hydrate, Gulf of Mexico
808 continental slope. *Organic Geochemistry*, *22*(6), 1029–1032. https://doi.org/10.1016/0146-
809 6380(94)90036-1

810 Sassen, R., Sweet, S. T., Milkov, A. V, Defreitas, D. A., Kennicutt, M. C., & Roberts, H. H.
811 (2001). Stability of Thermogenic Gas Hydrate in the Gulf of Mexico: Constraints on
812 Models of Climate Change. In C. K. Paull & W. P. Dillon (Eds.), *Natural Gas Hydrates:*
813 *Occurrence, Distribution, and Detection* (Geophys. M, pp. 131–143). AGU.
814 https://doi.org/10.1029/GM124p0131

815 Serié, C., Huuse, M., Schødt, N. H., Brooks, J. M., & Williams, A. (2017). Subsurface fluid flow
816 in the deep-water Kwanza Basin, offshore Angola. *Basin Research*, *29*(2), 149–179.
817 https://doi.org/10.1111/bre.12169

818 Shankar, U., Sain, K., & Riedel, M. (2014). Assessment of gas hydrate stability zone and
819 geothermal modeling of BSR in the Andaman Sea. *Journal of Asian Earth Sciences*,
820 *79*(PA), 358–365. https://doi.org/10.1016/j.jseaes.2013.10.021

821 Shipley, T. H., & Houston, M. H. (1979). Seismic Evidence for Widespread Possible Gas
822 Hydrate Horizons on Continental Slopes and Rises. *AAPG Bulletin*, *63*(12), 2204–2213.
823 https://doi.org/10.1306/2F91890A-16CE-11D7-8645000102C1865D

824 Sloan, E. D. (1990). Natural Gas Hydrate Phase Equilibria and Kinetics : Understanding the
825 State-Of-The-Art. *Revue de l'Institut Français Du Pétrole*, *45*(2), 245–266.
826 https://doi.org/10.2516/ogst:1990018

827 Sloan, E. D., Subramanian, S., Matthews, P. N., Lederhos, J. P., & Khokhar, A. A. (1998).
828 Quantifying Hydrate Formation and Kinetic Inhibition. *Industrial & Engineering Chemistry*
829 *Research*, *37*(8), 3124–3132. https://doi.org/10.1021/ie970902h

830 Thompson, K. F. . (1979). Light hydrocarbons in subsurface sediments. *Geochimica et*
831 *Cosmochimica Acta*, *43*(5), 657–672. https://doi.org/10.1016/0016-7037(79)90251-5

832 Vargas-Cordero, I., Tinivella, U., Accaino, F., Loreto, M. F., & Fanucci, F. (2010). Thermal state
833 and concentration of gas hydrate and free gas of Coyhaique, Chilean Margin (44° 30' S).
834 *Marine and Petroleum Geology*, *27*(5), 1148–1156.
835 https://doi.org/10.1016/j.marpetgeo.2010.02.011

Wang, C., Dong, S., & Munoz, E. (2010). Seawater density variations in the North Atlantic and the Atlantic meridional overturning circulation. *Climate Dynamics*, *34*(7–8), 953–968. https://doi.org/10.1007/s00382-009-0560-5

Wood, W. T., & Ruppel, C. (2000). Seismic and thermal investigations of the Blake Ridge gas hydrate area: A synthesis. In C. K. Paull, R. Matusmoto, P. J. Wallace, & W. P. Dillon (Eds.), *Proceedings of the Ocean Drilling Program: Scientific Results* (Vol. 164, pp. 253–264). https://doi.org/10.2973/odp.proc.sr.164.203.2000

Yamano, M., Uyeda, S., Aoki, Y., & Shipley, T. H. (1982). Estimates of heat flow derived from gas hydrates. *Geology*, *10*(7), 339. https://doi.org/10.1130/0091-7613(1982)10<339:EOHFDF>2.0.CO;2